Personalized computational modeling of left atrial geometry and transmural myofiber architecture

Thomas E. Fastl [a,*], Catalina Tobon-Gomez [a], Andrew Crozier [b], John Whitaker [a,c],
Ronak Rajani [a,c], Karen P. McCarthy [d], Damian Sanchez-Quintana [e], Siew Y. Ho [d],
Mark D. O'Neill [a,c], Gernot Plank [b], Martin J. Bishop [a], Steven A. Niederer [a]

[a] Department of Biomedical Engineering, King's College London, London, United Kingdom
[b] Institute of Biophysics, Medical University of Graz, Graz, Austria
[c] Department of Cardiology, Guy's and St Thomas' Hospitals, London, United Kingdom
[d] Cardiac Morphology Unit, Royal Brompton Hospital, London, United Kingdom
[e] Department of Anatomy and Cell Biology, University of Extremadura, Badajoz, Spain

ARTICLE INFO

ABSTRACT

Atrial fibrillation (AF) is a supraventricular tachyarrhythmia characterized by complete absence of co-ordinated atrial contraction and is associated with an increased morbidity and mortality. Personalized computational modeling provides a novel framework for integrating and interpreting the role of atrial electrophysiology (EP) including the underlying anatomy and microstructure in the development and sustenance of AF. Coronary computed tomography angiography data were segmented using a statistics-based approach and the smoothed voxel representations were discretized into high-resolution tetrahedral finite element (FE) meshes. To estimate the complex left atrial myofiber architecture, individual fiber fields were generated according to morphological data on the endo- and epicardial surfaces based on local solutions of Laplace's equation and transmurally interpolated to tetrahedral elements. The influence of variable transmural microstructures was quantified through EP simulations on 3 patients using 5 different fiber interpolation functions. Personalized geometrical models included the heterogeneous thickness distribution of the left atrial myocardium and subsequent discretization led to high-fidelity tetrahedral FE meshes. The novel algorithm for automated incorporation of the left atrial fiber architecture provided a realistic estimate of the atrial microstructure and was able to qualitatively capture all important fiber bundles. Consistent maximum local activation times were predicted in EP simulations using individual transmural fiber interpolation functions for each patient suggesting a negligible effect of the transmural myofiber architecture on EP. The established modeling pipeline provides a robust framework for the rapid development of personalized model cohorts accounting for detailed anatomy and microstructure and facilitates simulations of atrial EP.

1. Introduction

Atrial fibrillation (AF) is a supraventricular tachyarrhythmia characterized by uncoordinated atrial activation with consequent deterioration of mechanical function. Affecting an estimated 33 million people worldwide (Rahman et al., 2014), AF is the most common arrhythmia and is associated with an increased long-term risk of other cardiovascular diseases. Personalized computational modeling provides a novel framework for integrating and interpreting the role of electrophysiology (EP) in the development and progression of AF (Trayanova, 2014; Trayanova and Chang, 2016). Numerous atrial models of different species, varying complexity and diverse applications have been generated over the last decades and used to investigate medical questions, however, a processing pipeline for standardized generation of personalized atrial computer models remains unavailable (Seemann et al., 2006; Jernigan et al., 2007; Zhang and Gay, 2008; Hunter et al., 2012; Krueger et al., 2013; Gonzales et al., 2013; Satriano et al., 2013; Adeniran et al., 2015; Ferrer et al., 2015; Moyer et al., 2015; McDowell et al., 2015; Zhao et al., 2015; 2017; Varela et al., 2016). While

* Corresponding author.
E-mail address: thomas.fastl@kcl.ac.uk (T.E. Fastl).

an increased image resolution facilitates the generation of detailed anatomical models of the atria (Bishop et al., 2016; Pashakhanloo et al., 2016; Zhao et al., 2015; 2017), standardized assignment of the complex atrial myofiber architecture remains challenging. Computational studies in the atria have demonstrated the influence of structural anisotropy on EP substantiating the importance of the atrial fiber orientation in finite element (FE) simulations (Krueger et al., 2011; 2013; Ferrer et al., 2015).

Significant limitations of atrial *in vivo* imaging, due to its thin-walled phenotype, have motivated comprehensive anatomical and morphological *ex vivo* studies aiming to characterize the atrial fiber architecture qualitatively over the endo- and epicardial surfaces (Ho et al., 1999; 2002; Cabrera et al., 2008; Ho and Sánchez-Quintana, 2009). Additional *ex vivo* quantifications of the atrial fiber orientation include serial surface macroscopy (Zhao et al., 2012; 2013), micro-computed tomography (CT) (Varela et al., 2013; Zhao et al., 2015; Stephenson et al., 2017), diffusion tensor magnetic resonance imaging (MRI) (Pashakhanloo et al., 2016) and contrast-enhanced MRI (Zhao et al., 2017).

The majority of atrial modeling studies have incorporated the structural anisotropy using rule-based approaches to qualitatively represent observed fiber morphologies in the literature. Due to the complex structure of the atrial fiber architecture, however, applied rules have been manually attributed to specific atrial regions and structures (Harrild and Henriquez, 2000; Vigmond et al., 2001; Jacquemet et al., 2003; Seemann et al., 2006; Tobón et al., 2013; Gonzales et al., 2013; Ferrer et al., 2015; Moyer et al., 2015). Although the methods presented in the individual studies have appropriately reflected the underlying atrial fiber distribution, these approaches are not suitable for large patient cohorts. To generate personalized computational models of the atria including the fiber orientation for multiple patient geometries, a variety of rule-based semi-automatic approaches have been proposed (Werner et al., 2000; Hermosillo, 2008; Krueger et al., 2011; Labarthe et al., 2012; Satriano et al., 2013). Furthermore, atlas-based methods, in which a number of distinct landmarks are used to warp an existing atrial fiber orientation defined on a source geometry onto a particular target geometry, are becoming increasingly popular (McDowell et al., 2012; 2013; Satriano et al., 2013; McDowell et al., 2015). Both techniques estimate the atrial fiber architecture, however, manual intervention will increase intra- and interobserver variability as well as limit reproducibility. At present there are no clinically applicable automated methods to either generate anatomically detailed personalized atrial computer geometries or reliably estimate the atrial fiber architecture *in vivo*.

An integrative pipeline to generate personalized computational models of the left atrium (LA) suitable for FE simulations of atrial EP is presented in this article. Statistics-based image segmentation of high-resolution coronary CT angiography (CTA) data was performed and the smoothed voxel representations subsequently discretized into high-resolution and high-fidelity tetrahedral FE meshes. Morphological data informed the qualitative estimation of the complex left atrial fiber architecture, primarily based on local solutions of Laplace's equation. The automated modeling pipeline was exercised on 3 patient cases, while electrophysiological FE simulations were performed to analyze the influence of the transmural tissue microstructure on the local activation time (LAT).

2. Methods

The automated modeling pipeline for generating detailed personalized computational models of the LA is illustrated in Fig. 1. Preliminary results have been published in Fastl et al. (2016). All details for the proposed algorithm are provided in this paper. Retrospective analysis of 3 patient cases (see Table 1 for baseline demographics) who underwent a clinically indicated coronary CTA

Table 1
Baseline demographics for retrospectively analyzed patient cohort. Abbreviations: M (male), F (female), HLD (hyperlipidemia), PAF (paroxysmal atrial fibrillation) and SSS (sick sinus syndrome).

	Sex	Age [yr]	Comorbidities
Patient I	M	35	HLD
Patient II	F	48	NIL
Patient III	F	54	PAF, SSS

to exclude coronary artery disease was performed to exercise the proposed atrial modeling pipeline. Selected personalized computational models of the LA including the estimated fiber architectures are available online (http://doi.org/doi:10.18742/RDM01-289).
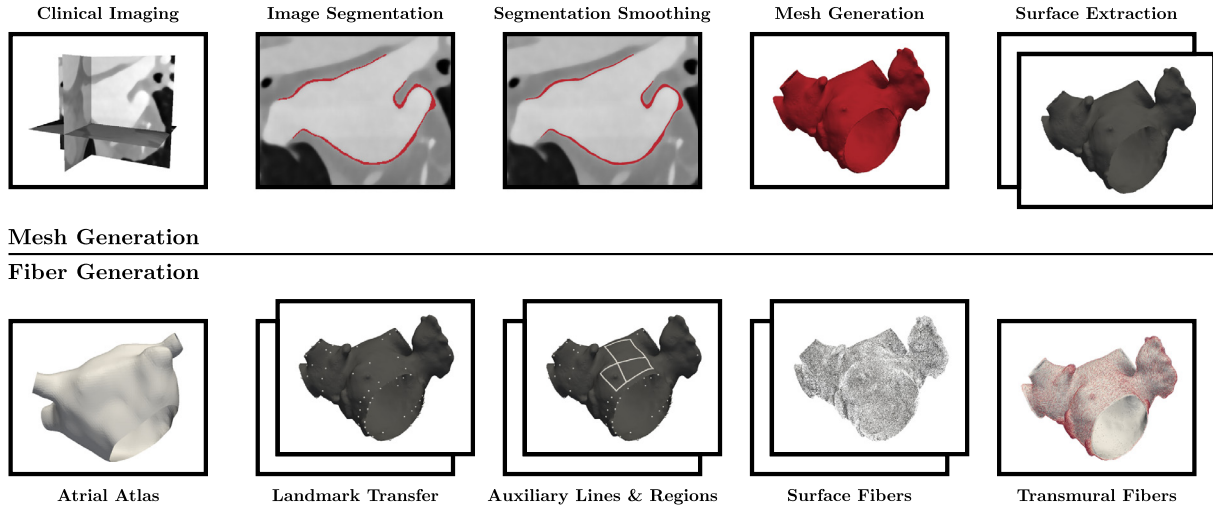
2.1. Clinical imaging

The applied coronary CTA protocol has been described previously in Bishop et al. (2016). Briefly, coronary CTA data were acquired at Guy's and St Thomas' NHS Foundation Trust using a Philips 256 iCT scanner (Philips Healthcare, Amsterdam, Netherlands). The acquired coronary CTA data were reconstructed at 75% of the RR interval (most likely corresponding to the left atrial conduit phase) using an iterative reconstruction (iDose level 4) with 0.80 mm slice thickness, 0.40 mm slice increment, 250.00 mm field of view (approximate size), 512×512 matrix and a smooth reconstruction kernel (Donal et al., 2016).

2.2. Image segmentation

Based on the assumption of comparable radiodensities in the atrial and ventricular myocardium (Bishop et al., 2016), a regionally tagged segmentation of the LA was generated using the software package Seg3D (Center for Integrative Biomedical Computing, 2016). Within the image space 3 sample regions of approximately equal size were selected in both the left ventricular myocardium and the left atrial cavity, for which combined mean values and standard deviations were calculated (see voxel intensity histograms including calculated thresholds in Fig. A1). Coronary CTA images were processed using a 4-point median filter to enhance the image contrast and manually cropped to encapsulate the LA and reduce unnecessary computational overhead. The left atrial myocardium and the left atrial blood pool were thresholded utilizing their corresponding statistical sample mean value reduced or increased by 3 times the sample standard deviation, respectively. The continuous transition between the left atrial myocardium and the left atrial blood pool required a common threshold value chosen as the average of both statistical mean values of the combined sample regions. Furthermore, the viable left atrial myocardium was restricted to a maximum thickness of 3 mm to separate any neighboring structures, e.g., right and left ventricles, right atrium, aorta and coronary sinus, with similar Hounsfield units (Dössel et al., 2012; Whitaker et al., 2016).

Initial dilation of the segmented left atrial blood pool by 1 voxel was performed to obtain a minimum wall thickness. The subsequent iterative dilations combined with logical operations ($\cap$) on the viable atrial myocardium provided the raw segmentation of the left atrial wall. Some minor cosmetic operations, e.g., smoothing and filling operations, were applied to obtain the final segmentation of the left atrial myocardium Ω_{MC}. Standardized mitral valve (MV) exclusion was performed utilizing a binary spherical shell Ω_{SS} generated by manual specification of 3 points around the MV annulus and removal of voxels distal from the LA. Pulmonary veins (PVs) were cropped using multiple binary cylindrical disks $\Omega_{CD} = \sum_{i=1}^{n} \Omega_{CD}^i$, with $i = 1, \ldots, n$, where n is the number of PVs

Clinical Imaging　　Image Segmentation　　Segmentation Smoothing　　Mesh Generation　　Surface Extraction

Mesh Generation

Fiber Generation

Atrial Atlas　　Landmark Transfer　　Auxiliary Lines & Regions　　Surface Fibers　　Transmural Fibers

Fig. 1. Personalized computational modeling pipeline for left atrial electrophysiology separated into the mesh generation phase (top) and the subsequently performed fiber generation phase (bottom). Individual boxes illustrate representative generation processes, while two boxes indicate processes on multiple surfaces, i.e., endo- and epicardium.

present, by manual identification of 3 points on each vein *i* and removal of voxels distal from the LA. Both geometries, the spherical shell as well as the cylindrical disks, were subsequently employed to generate tags for the MV annulus, i.e., $\Omega_{MV} = \Omega_{MC} \cap \Omega_{SS}$, and the ends of the PVs, i.e., $\Omega_{PV} = \Omega_{MC} \cap \Omega_{CD}$, while the representation of the left atrial wall becomes $\Omega_{AW} = [\Omega_{MC} \oplus (\Omega_{MV} \cup \Omega_{PV})]$, with $\oplus$ denoting the XOR operation.

2.3. Segmentation smoothing

A combined smoothing and upsampling algorithm was applied to the anatomically tagged voxel representation attenuating staircase effects and providing an isotropic segmentation with sufficient spatial resolution for computational FE mesh generation (Crozier et al., 2016). While a variational method was employed to correct for low resolution artifacts of the surface, smoothing was achieved by minimization of a high-order penalty restricting the maximum displacement of the reference surface to 50% of the voxel size ensuring that the resulting isosurface is within the error margin of the imaging modality. The resulting surface encompassing the left atrial geometry was resampled providing an image segmentation with a consistently isotropic 100 μm voxel resolution.

2.4. Mesh generation

A high-fidelity and high-resolution mesh of the LA was created using the Octree-based mesh generation software Tarantula (CAE Software Solutions, Eggenburg, Austria), which builds unstructured and locally refined tetrahedral FE meshes and maps classification tags from the input segmentation onto the generated mesh. Identification of the endo- and epicardium including the corresponding surface meshes of the LA relied on a breadth-first search algorithm implemented in MATLAB (The MathWorks, Inc., Natick, United States).

2.5. Image registration

A major advantage of the proposed method to generate detailed personalized computational models of the LA including the complex fiber architecture is the automated transfer of predefined landmarks from an average atrial geometry to the personalized atrial geometry. This average atrial geometry was generated by combination of 30 MRI datasets and manual segmentation of the endocardium (Tobon-Gomez et al., 2015).

Endo- and epicardial surface meshes were decimated to approximately 10% of the reference element number using the Computational Geometry Algorithms Library facilitating a tractable image registration (Cacciola, 2017). The resulting surface meshes were manually initialized to match the average atrial geometry and subsequently registered using the software Deformetrica (Durrleman et al., 2014). A nearest neighbor approach was applied to transfer 122 predefined landmarks on the average atrial geometry to the corresponding decimated and registered surface mesh (the maximum potential mapping error, the average distance between nodes of the atrial atlas and the nearest nodes on the registered surface meshes of all patients, was evaluated as 0.52 mm, approximately equal to the image resolution). During the image registration process the mesh topology was maintained, hence a final nearest neighbor transfer of the landmarks from the decimated to the personalized atrial surface meshes provided their location. An additional 62 landmarks were calculated around the PVs, MV, left atrial appendage (LAA) and interatrial septum using the spatial information of already transferred landmarks. Minor manual adjustment of individual landmarks around the PVs, MV and LAA was performed where necessary as a consequence of the large structural variability.

2.6. Surface fiber generation

Landmarks on the left atrial surfaces constituted a predefined network of 272 auxiliary lines, which subdivided both endo- and epicardial surfaces into 151 atrial regions (see Fig. 2) similar to the approaches in Hunter et al. (2012) and Teh et al. (2012). The auxiliary lines were calculated using an implementation of the Dijkstra algorithm applied on preselected corridors utilizing the geodesic paths between the corresponding landmarks. Then, a region growing algorithm identified the atrial regions Ω, on which Laplace's equation

$$\nabla^2 u = 0 \tag{1}$$

was solved within the Cardiac Arrhythmia Research Package (Vigmond et al., 2003) using boundary conditions applied to $\partial\Omega_I$, $\partial\Omega_{II}$ and $\partial\Omega_R$ representing the bordering auxiliary lines (see Fig. 2), i.e.,

$$u|_{\partial\Omega_I} = 0, \qquad u|_{\partial\Omega_{II}} = 1, \qquad \frac{\partial u}{\partial\mathbf{n}}\bigg|_{\partial\Omega_R} = 0. \tag{2}$$

The normalized gradient of the obtained scalar field $\nabla u/\|\nabla u\|$ evaluated at the surface triangle centers represented the modeled
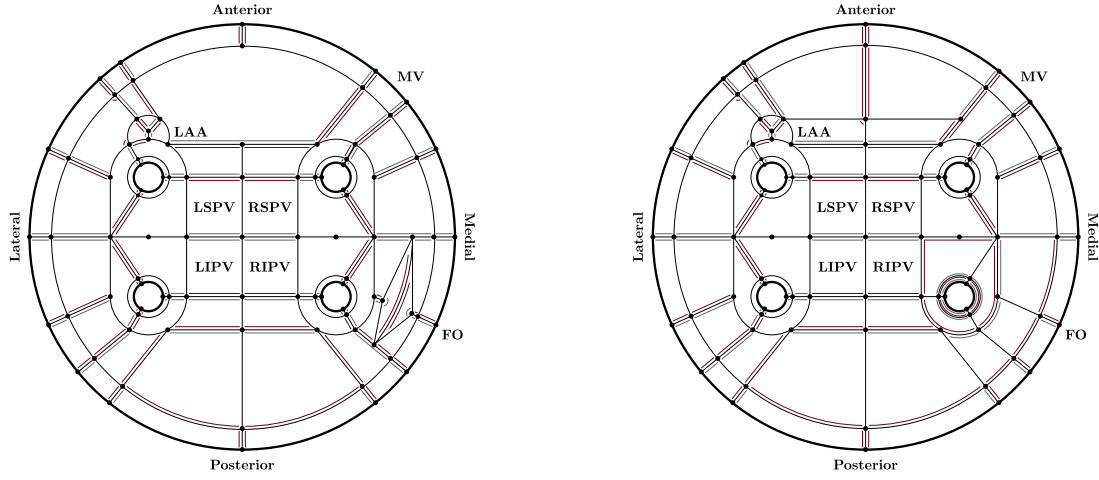
Fig. 2. Idealized unfolded representation of the endo- (left panel) and epicardial (right panel) surfaces of the left atrium indicating individual landmarks (only constituting landmarks of auxiliary lines are provided), auxiliary lines and atrial regions. Boundary conditions to generate regional surface fibers are provided in red and gray corresponding to (2.1) and (2.2), respectively, while (2.3) was applied to any remaining boundary. Abbreviations: LAA (left atrial appendage), MV (mitral valve), FO (fossa ovalis), RSPV (right superior pulmonary vein), RIPV (right inferior pulmonary vein), LSPV (left superior pulmonary vein) and LIPV (left inferior pulmonary vein). (For interpretation of the references to colour in this figure legend, the reader is referred to the web version of this article.)

fiber orientation and estimated the morphologically observed atrial fiber architecture. The calculated fiber vectors were complemented with the fiber vectors of adjacent elements where necessary to obtain a full representation of the personalized fiber field on the endo- and epicardial surfaces of the LA. Interregional fiber smoothing using an orientation-based neighborhood approach was applied to triangular elements in the proximity of the auxiliary lines. Finally, out-of-plane fibers due to the smoothing procedure were projected onto the tangential plane of the atrial surface followed by vector normalization.

### 2.7. Transmural fiber generation

Fiber direction vectors for tetrahedral elements were obtained by transmural interpolation (see Fig. 3) of the estimated surface fiber field according to a correspondence map. Therefore, (1) was solved on the tetrahedral FE mesh Ω with boundary conditions in (2) applied to $\partial\Omega_I$, $\partial\Omega_{II}$ and $\partial\Omega_R$ representing the endocardial, epicardial and remaining boundary surfaces, respectively. Starting from the tetrahedral element center, endo- and epicardial surface triangles were identified by tracking the unit field lines evaluated as $\nabla u / \|\nabla u\|$. An element average of the nodal solutions u representing the normalized transmural location ϕ was calculated and utilized to evaluate an interpolation weight ω_j, where j represents a mathematical function as defined below.

The influence of variable transmural microstructures on LAT was quantified using 4 different transmural interpolation functions ω_j graphically shown in Fig. 3. Since anatomical and morphological studies have indicated a multi-layer structure within the left atrial myocardium, though the exact number of layers remains unknown, 2-layer (3), 5-layer (4), linear (5) and sigmoidal (6) transmural fiber interpolation functions were chosen given as

$$\omega_1(\phi) = \begin{cases} 0.00 & \text{if } \phi \leq 0.50 \\ 1.00 & \text{if } \phi > 0.50 \end{cases}, \tag{3}$$

$$\omega_2(\phi) = \begin{cases} 0.00 & \text{if } \phi \leq 0.20 \\ 0.25 & \text{if } 0.20 < \phi \leq 0.40 \\ 0.50 & \text{if } 0.40 < \phi \leq 0.60, \\ 0.75 & \text{if } 0.60 < \phi \leq 0.80 \\ 1.00 & \text{if } \phi > 0.80 \end{cases} \tag{4}$$

$$\omega_3(\phi) = \phi, \tag{5}$$
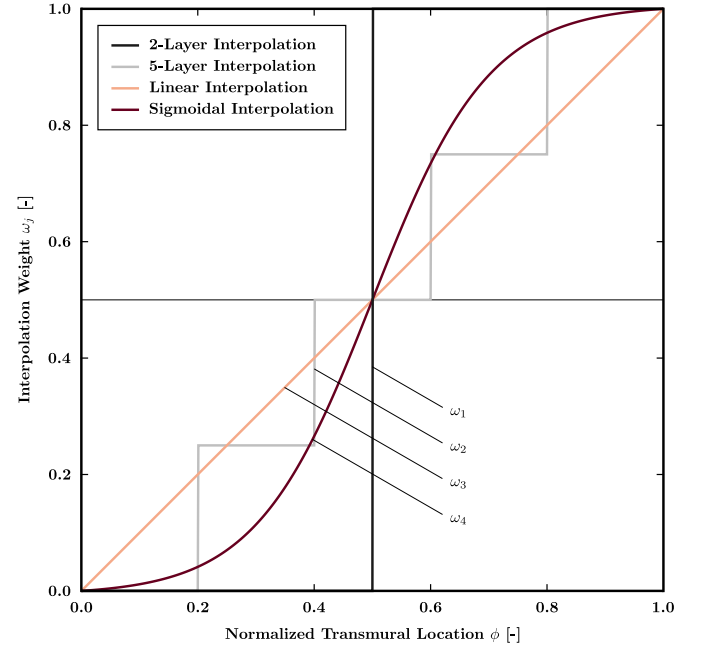
Fig. 3. Employed fiber interpolation functions providing an interpolation weight ω_j for each tetrahedral element dependent on the normalized transmural element location ϕ evaluated at the tetrahedral element center.

$$\omega_4(\phi) = \frac{1}{2}\tanh(5(\phi - 0.5)), \tag{6}$$

respectively, where tanh represents the hyperbolic tangent. The fiber direction in all tetrahedral elements was assigned based on the estimated direction vectors of the corresponding surface triangles according to

$$\mathbf{f}^i = \frac{(1 - \omega_j^i)\mathbf{f}_{ED}^i + \omega_j^i\mathbf{f}_{EP}^i}{\|(1 - \omega_j^i)\mathbf{f}_{ED}^i + \omega_j^i\mathbf{f}_{EP}^i\|}, \tag{7}$$

where $\mathbf{f}_{ED}^i$ and $\mathbf{f}_{EP}^i$ denote the surface fiber direction vectors on the endo- and epicardium for element i, respectively. Finally, all tetrahedral element fiber direction vectors were projected onto a plane orthogonal to the associated unit field line.

Table 2

Clinical imaging, image segmentation and mesh generation characteristics for retrospectively analyzed patient models. The voxel dimensions VD (prior to segmentation smoothing and upsampling) depend on the chosen imaging parameters. The segmentation intensity thresholds LT, MT and UT represent the lower, mid and upper thresholds to identify the left atrial myocardium and the left atrial cavity, respectively. Finite element mesh properties including the number of nodes $\#_{\text{nodes}}$, number of elements $\#_{\text{elements}}$, mesh volume VL and average element edge length EL are provided.

	VD [mm]	LT [HU]	MT [HU]	UT [HU]	$\#_{\text{nodes}}$ [–]	$\#_{\text{elements}}$ [–]	VL [cm³]	EL [µm]
Patient I	$0.35 \times 0.35 \times 0.40$	52.26	223.97	484.26	21, 868, 400	121, 207, 799	18.05	120.72
Patient II	$0.25 \times 0.25 \times 0.40$	63.74	330.01	628.88	14, 352, 781	79, 067, 310	11.79	120.84
Patient III	$0.39 \times 0.39 \times 0.40$	89.04	314.27	566.27	8, 736, 713	46, 154, 317	6.43	116.85

2.8. Electrophysiology simulations

In all patients cellular EP was described using the Courtemanche–Ramirez–Nattel (CRN) model to simulate the human atrial action potential (Courtemanche et al., 1998). The intracellular current flow responsible for the spread of electrical activation in the atrial myocardium was calculated using the monodomain equation

$$\beta_{\text{m}} C_{\text{m}} \frac{dV_{\text{m}}}{dt} + \beta_{\text{m}} I_{\text{ion}}(V_{\text{m}}, \boldsymbol{\eta}) = \nabla \cdot (\boldsymbol{\sigma}_{\text{m}} \nabla V_{\text{m}}) + I_{\text{tr}}, \qquad (8)$$

where β_{m} is the membrane surface-to-volume ratio, C_{m} is the membrane capacity, V_{m} is the transmembrane potential, I_{ion} is the density of the total ionic currents as a function of V_{m} and a set of state variables $\boldsymbol{\eta}$, I_{tr} is a transmembrane stimulus current and $\boldsymbol{\sigma}_{\text{m}}$ represents the monodomain conductivity tensor. Single cell stimulation on the standard CRN model using 1000 beats with a basic cycle length of 1000 ms was performed prior to EP simulations to obtain steady state conditions. The conduction velocities in the LA were chosen as 1.20 and 0.40 m/s in longitudinal and transversal direction, respectively, leading to an anisotropy ratio of 3/1, well within the range of reported values for healthy patients (Dimitri et al., 2012; Zemlin et al., 2001). To match the reported conduction velocities in the EP simulations, the monodomain conductivity tensor $\boldsymbol{\sigma}_{\text{m}}$ was iteratively fitted using the method described in Mendonca Costa et al. (2013). The Cardiac Arrhythmia Research Package was employed to numerically solve (8) via the FE method using a global time step of 10 µs (Vigmond et al., 2008). Regionally confined epicardial stimulation around the Bachmann's bundle (BB) was applied to mimic the physiological signal transduction from the right atrium (Markides et al., 2003). The LAT was recorded once the transmembrane potential V_{m} exceeded a threshold of -20 mV. Besides anisotropic EP simulations utilizing the 4 different transmural microstructures introduced, an isotropic reference EP simulation was performed for each patient. To model the non-physiological isotropic electrical material, the anisotropic monodomain conductivity tensor $\boldsymbol{\sigma}_{\text{m}}$ was combined with a random fiber architecture.

3. Results

The automated personalized modeling pipeline was exercised on 3 patient cases (see Table 1) to demonstrate its ability to generate detailed FE models including a qualitative representation of the left atrial fiber architecture. The influence of a variable transmural microstructure utilizing different transmural fiber interpolation functions on the LAT was quantified using electrophysiological FE simulations.

3.1. Computational model generation

Acquired coronary CTA images (see Table 2 for voxel dimensions) were retrospectively analyzed and voxel intensity histograms of the combined 6 individual sample regions selected within the left atrial blood pool and the left ventricular myocardium for individual patients are presented in Fig. A1. Based on the obtained histograms, personalized intensity thresholds for the left atrial myocardium and the left atrial cavity were calculated and are specified in Table 2. Furthermore, important characteristics on the generated high-fidelity and high-resolution FE meshes are presented in Table 2. While consistent average element edge lengths of approximately 120 µm were achieved in all patients due to isotropic segmentation resampling, a large variation in myocardial tissue volume (assumed as the volume of the FE mesh) between patients was observed. This explained the large differences in node and element numbers between individual patients.

3.2. Estimated fiber architecture

The novel algorithm to estimate the left atrial fiber architecture qualitatively captured the complex arrangement of fiber bundles in the LA. Although interpatient variation has been observed in morphological images, the predominant features of the left atrial fiber architecture are preserved.

The atrial fiber structure on the anterior endocardium was dominated by the septoatrial bundle ascending oblique from the anterior interatrial raphe. The septoatrial bundle split up into 3 major fascicles to encircle the LAA and combine with longitudinal fibers at the posterior portion of the LA between the PVs (see top left comparison in Fig. 4). Endocardial fibers at the PV orifices transferred into a circular fiber arrangement around all PVs, while circular fibers were also observed around the MV and the LAA (see bottom left comparison in Fig. 4). An elliptical fiber orientation was obtained at the left atrial portion of the interatrial septum representing the fossa ovalis (FO).

The atrial fiber structure on the anterior epicardium was dominated by the septopulmonary bundle (see top right comparison in Fig. 4) and the BB. While the fascicles of the BB, which ran parallel to the atrioventricular groove, encircled the LAA, oblique and longitudinal fibers of the septopulmonary bundle proceeded longitudinally at the posterior wall of the LA besides fanning out to entwine the PVs. Similar to the endocardium, circular fiber arrangements were observed around the PVs, with the exception of longitudinal fibers at the right inferior PV (RIPV) (see top right comparison in Fig. 4), MV and LAA (see bottom right comparison in Fig. 4) on the epicardium. The complex epicardial region around the FO was simplified, hence a longitudinal fiber orientation was obtained.

3.3. Electrophysiology simulations

Latest activation in all patients occurred in the isotropic reference simulation with maximum LATs of 111.31, 106.43 and 88.95 ms for Patients I, II and III, respectively. When only considering the anisotropic EP simulations, maximum LATs of 102.60 and 86.11 ms were observed utilizing the linear transmural fiber interpolation function $\omega_3(\phi)$ in Patients I and III, respectively, while in Patient II a maximum LAT of 85.62 ms was predicted using the 2-layer transmural fiber interpolation function $\omega_1(\phi)$.
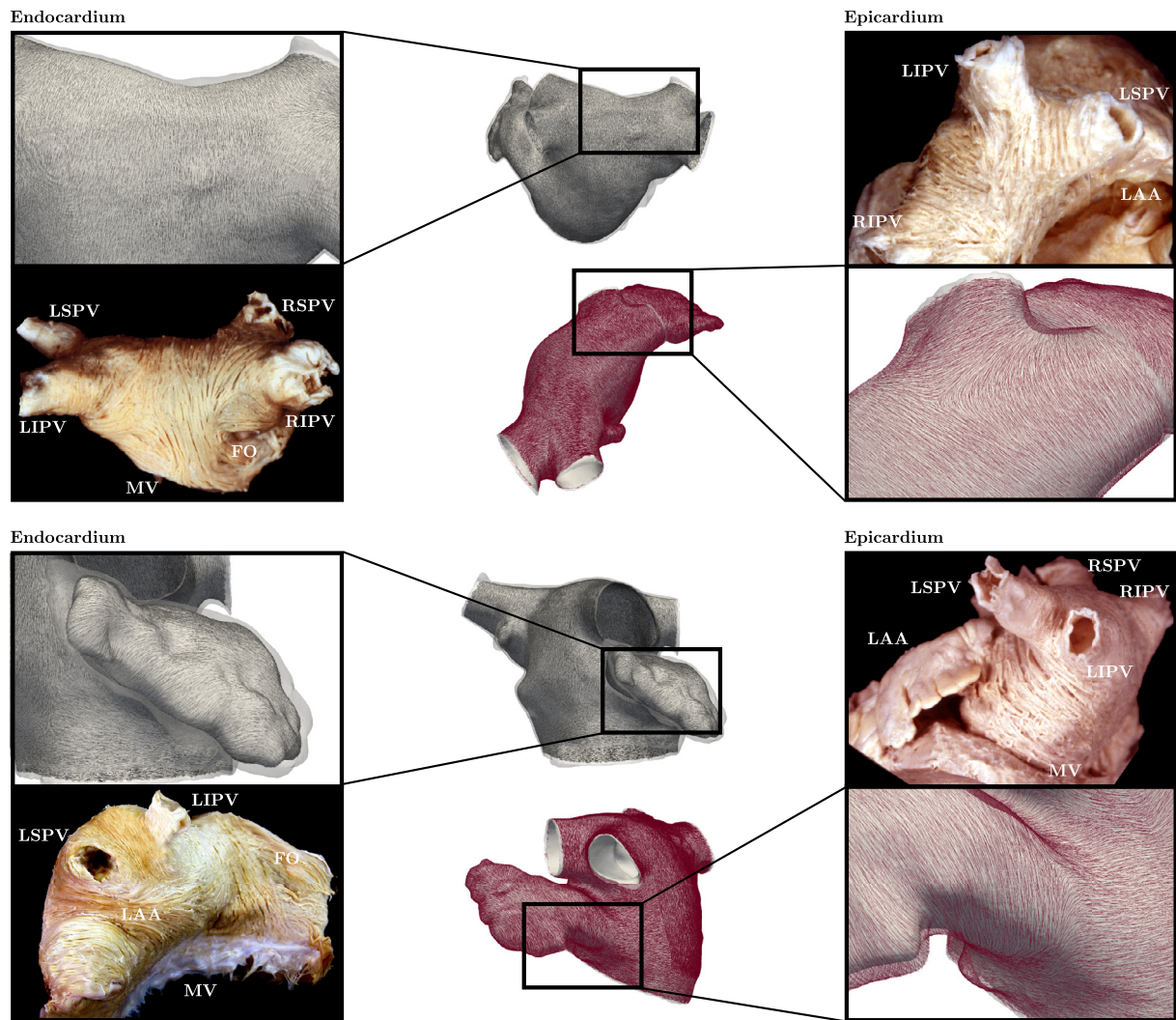
Fig. 4. Comparison between modeled left atrial fiber orientation in Patient III and morphological images on the endocardium (left panel), shown in everted and horizontally flipped state (cf., e.g., Ho et al. (1999) and Cabrera et al. (2008)), and the epicardium (right panel). Specifically, comparisons on the endocardial posterior region (top left), the endocardial left atrial appendage (bottom left), the epicardial posterior region including the pulmonary veins (top right) and the epicardial lateral region (bottom right) are shown. Abbreviations: LAA (left atrial appendage), MV (mitral valve), FO (fossa ovalis), RSPV (right superior pulmonary vein), RIPV (right inferior pulmonary vein), LSPV (left superior pulmonary vein) and LIPV (left inferior pulmonary vein).

Fig. 5 provides the individual differences in LATs between the anisotropic EP simulations using the different transmural interpolation functions and the isotropic reference simulation; symbols ⋆, ♦, ♠ and ♣ denote the LAT differences between the 2-layer, 5-layer, linear and sigmoidal interpolation simulations compared to the isotropic simulation, respectively. The maximum range of LAT differences was consistently observed between the anisotropic simulation using the linear interpolation function $\omega_3(\phi)$ and the isotropic reference simulation. These ranges were calculated as 58.98, 55.04 and 47.61 ms for Patients I, II and III, respectively. The regional activation times, an average of LATs within specific regions, were calculated at the myocardial sleeves of the PVs on the endocardium and epicardium, where only small differences were observed as a consequence of the relatively thin myocardial wall. The EP models predicted ranges of 41.11–45.98, 40.93-51.41, 42.52–58.18 and 55.26–76.07 ms for the right superior PV (RSPV), RIPV, left superior PV (LSPV) and left inferior PV (LIPV), respectively, where an increasing range corresponds to an increasing distance of the specific region from the initial stimulation site.

Fig. 6 shows the anterior and posterior perspective of the anisotropic 2-layer simulation and the isotropic reference simulation for analyzed patients color-coded according to the calculated LAT. Isochrones of the LAT are provided in 10 ms intervals indicating large differences in the LAT and activation wave front shape between both EP simulations. While the isotropic reference simulation showed a circular spread of electrical activation around the stimulus region, the effect of the myocardial fiber arrangement became apparent in the anisotropic simulation leading to an elliptical activation spread. Moreover, the activation wave front exhibited a skewed shape due to different fiber directions on the endo- and epicardium.

4. Discussion

In this study, a novel pipeline to generate detailed personalized computational models for left atrial EP requiring a minimum degree of manual intervention was presented. A statistics-based segmentation algorithm identified the left atrial myocardium in coronary CTA images and enabled the generation of geometrical models
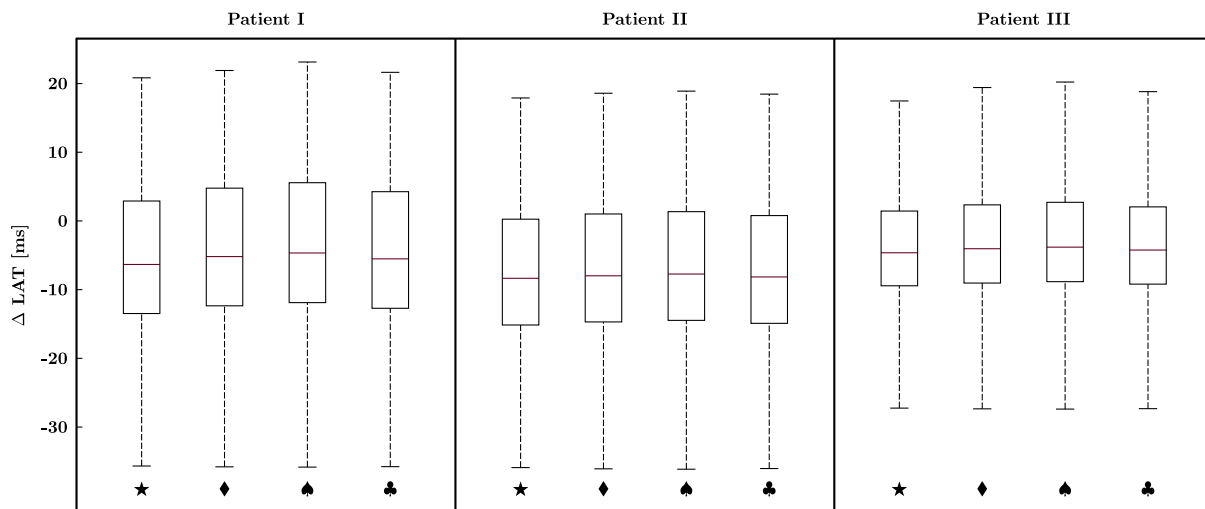
Fig. 5. Differences in local activation times between the anisotropic electrophysiology simulations and the isotropic reference simulation within all patients; symbols ⋆, ♦, ♠ and ♣ indicate differences between the 2-layer, 5-layer, linear and sigmoidal interpolation simulations compared to the isotropic simulation, respectively. Boxes in the figure indicate the first and third quartile, while the red line represents the second quartile and the whiskers indicate the data range. (For interpretation of the references to colour in this figure legend, the reader is referred to the web version of this article.)

with a varying myocardial thickness, for which a Laplace-based algorithm estimating the complex atrial fiber architecture was proposed. The modeling pipeline was applied to 3 patients and the impact of a transmurally varying fiber orientation on simulated LATs was quantified.

4.1. Computational model generation

The proposed statistics-based atrial segmentation algorithm extends on the method previously introduced in Bishop et al. (2016) by standardized determination of threshold values for each patient. Conventional segmentation algorithms for the atria have focused on the identification of the atrial cavity not labeling the atrial myocardium. Several studies have targeted and analyzed MRI with a relatively low image resolution $(1 - 2$ mm$)$ when compared to the thickness of the myocardial wall in the LA $(0.5 - 3$ mm$)$, which has made the segmentation of these images challenging (Whitaker et al., 2016), although recent progress has been made (Varela et al., 2017). As histograms in Fig. A1 indicate, the voxel intensity distributions of the ventricular myocardium are consistent across the 3 patient cases and well within the range reported for contrast-enhanced CT images (Ahn et al., 2009; Rodríguez-Granillo et al., 2010). Furthermore, a large intra- and interpatient variability, i.e., histograms exhibiting bimodal characteristics, in voxel intensities was observed in the blood pool reflecting a varied contrast agent concentration. This artifact results from the coronary CTA imaging acquisition, specifically from the image reconstruction, in which the voxel image was generated over the course of typically 2 consecutive heart beats changing the intensity of the contrast agent as it was pumped through the circulatory system. An identical threshold value MT was necessary in the image segmentation to obtain a continuous transition at the endocardial surface between the atrial myocardium and the contrast agent filled atrial cavity. While the lower threshold LT significantly influences the detection of viable atrial myocardium, the upper threshold UT removes structures with higher radiodensity, e.g., the vertebrae. The statistics-based image segmentation algorithm proposed herein is the first to account for the interimage variability in atrial myocardium and blood pool intensities.

Through recent progress in medical imaging and image analysis a variety of geometrical models of the LA have been gener-

ated (Seemann et al., 2006; Jernigan et al., 2007; Zhang and Gay, 2008; Hunter et al., 2012; Krueger et al., 2013; Gonzales et al., 2013; Satriano et al., 2013; Adeniran et al., 2015; Ferrer et al., 2015; Moyer et al., 2015; McDowell et al., 2015; Zhao et al., 2015; 2017; Varela et al., 2016). While in the majority of computational left atrial models a completely homogeneous or regionally homogeneous myocardial wall thickness has been assumed, only more recent studies have incorporated the variation in left atrial wall thickness (Seemann et al., 2006; Adeniran et al., 2015; Zhao et al., 2015; 2017; Varela et al., 2017). In this study the first left atrial models derived from high-resolution clinical patient data with a heterogeneous distribution of myocardial wall thickness were presented. Considering the transmural variation in myocardial fiber orientation, the left atrial wall thickness represents an important structural parameter in EP (Labarthe et al., 2013). As a consequence of the detailed representation of the left atrial myocardium, unstructured high-resolution and high-fidelity meshes of the LA were generated adopting the methods in Bishop et al. (2010) and Crozier et al. (2016). The increased FE mesh resolution reduces the numerical error in conduction velocity (Niederer et al., 2011), particularly important in fibrillation studies. The tetrahedral FE mesh volumes reported in Table 2 provide an approximation of the myocardial volume in the LA and exhibit large interpatient variation. The obtained values are consistent with the volumes of the original image segmentations showing errors smaller than 1.71%. Zhao et al. (2017) computed the left atrial tissue volume of a human female cadaver as 30.70 cm^3 utilizing *ex vivo* contrast-enhanced MRI. The differences to measurements in Table 2 could potentially be explained by the differences in left atrial wall thickness observed when measured using different imaging modalities (Whitaker et al., 2016).

4.2. Fiber generation algorithm

The major advantage of the proposed method to generate detailed personalized fiber architectures in computational models of the LA over existing approaches is the high degree of automation. Although rule-based and atlas-based approaches presented in the literature reflect the underlying myocardial fiber orientation (Werner et al., 2000; Hermosillo, 2008; Krueger et al., 2011; Labarthe et al., 2012; Satriano et al., 2013; McDowell et al., 2012),
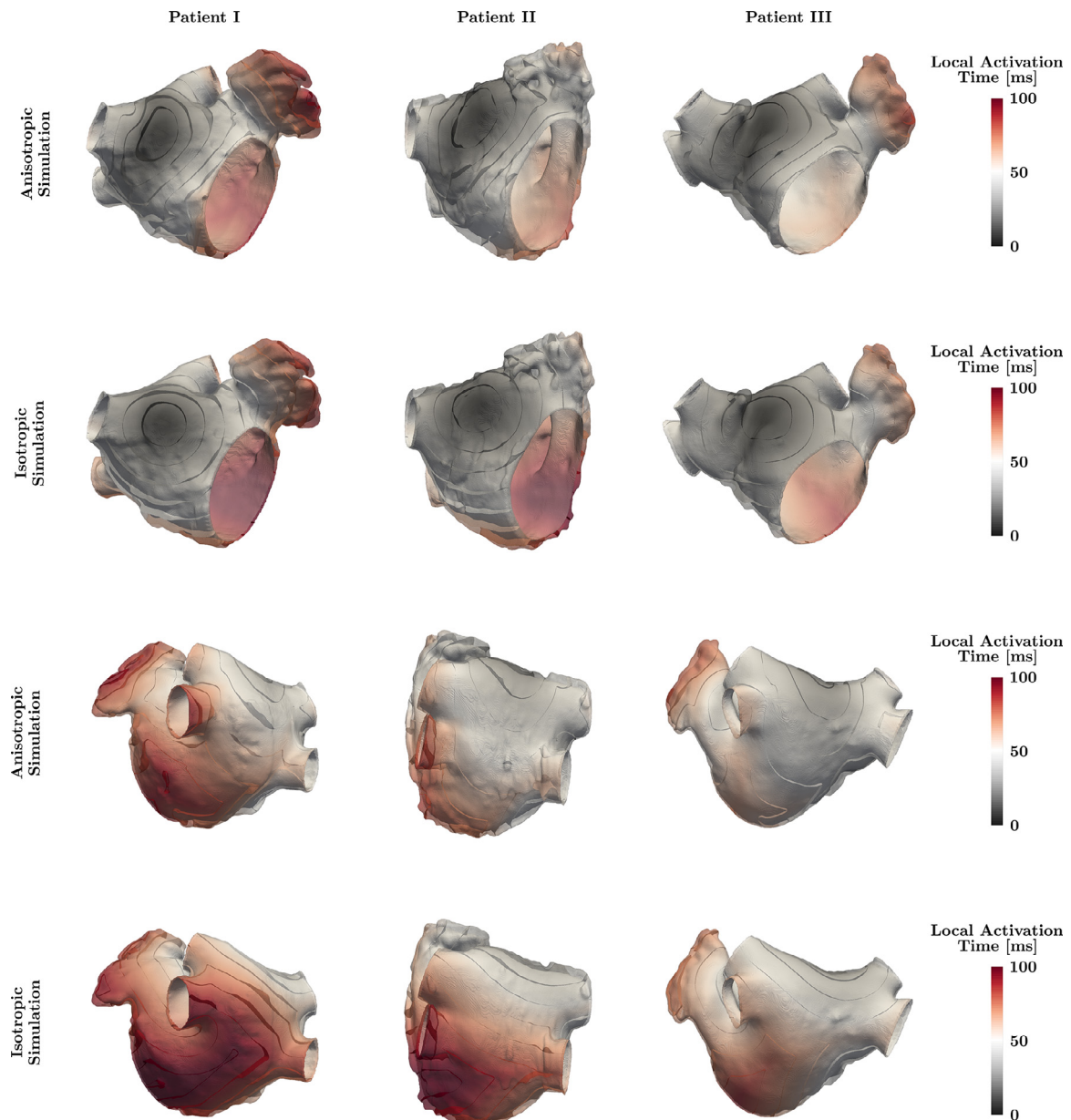
Fig. 6. Anterior (top rows) and posterior (bottom rows) perspective of analyzed patients showing the local activation time for isotropic and anisotropic electrophysiology simulations utilizing the 2-layer transmural fiber interpolation scheme $\omega_1(\phi)$. Isochrones are provided in 10 ms intervals and individual patient images are not to scale.

they suffer from either increased intra- and interobserver variability as well as limited reproducibility or are not suited for large patient cohorts. The novel method presented herein combines the advantages of both approaches using an automated transfer of predefined landmarks from an average atrial geometry to a personalized atrial geometry and *a priori* definition of certain rules to generate fibers. This combination of individual ideas results in a standardized procedure providing more consistent estimates of the left atrial fiber architecture. Moreover, the novel approach facilitates the consistent development of both surface and volume fibers for which specific transmural interpolation functions can be applied.

The visual comparison between the estimated left atrial fiber architecture and the morphological images in Fig. 4 illustrates a qualitative structural correspondence for all major fiber bundles. Although difficult, qualitative similarities in key regions

are observed when the estimated *in vivo* left atrial fiber architectures obtained using the proposed algorithm are visually compared to fiber architectures reported in the literature obtained using *ex vivo* imaging modalities. The estimated left atrial myofiber orientations qualitatively match the calculated left atrial myofiber orientations in the posterior regions reported in Zhao et al. (2015) and Zhao et al. (2017) derived from a single specimen using micro-CT and contrast-enhanced MRI, respectively. Pashakhanloo et al. (2016) characterized the left atrial myofiber architecture using diffusion tensor MRI in 8 specimens revealing consistent topologies for the major bundle structures with the estimated left atrial myofiber architecture. Moreover, Pashakhanloo et al. (2016) reported on the detailed transmural variation of fiber angles in 2 specimens utilizing 4 different regions of interest concluding either a 2-layer myofiber structure or no transmural myofiber variation.

4.3. Electrophysiology simulations

The performed EP simulations predicted consistently longer maximum LATs for the isotropic reference simulations when compared to anisotropic simulations. The alignment of the fiber orientation with the activation direction leads to faster anisotropic simulations, consistent with findings in Krueger et al. (2011) and Krueger et al. (2013) comparing a homogeneous isotropic and a heterogeneous anisotropic biatrial model. Similar LATs for anisotropic simulations using different transmural fiber interpolation functions within each patient suggest a negligible effect of the transmural fiber architecture on the activation pattern. The obtained maximum LATs in all patients for physiological conditions, i.e., anisotropic EP simulations, were slightly longer than clinically measured LATs in the LA for patients with an AF history (cf., e.g., 86 ± 19, 81 ± 10 and 75.4 ± 16.6 ms in Lemery et al. (2007), Chang et al. (2007) and Choi et al. (2010), respectively). This could potentially be explained by either the insufficient resolution in clinical measurements, particularly in the LAA, or the assumptions of using a single stimulus site as well as homogeneous cellular and tissue properties in EP simulations. Moreover, AF-induced electrical and structural remodeling can prolong the maximum LAT in the LA (Schotten et al., 2011). The calculated regional activation time ranges correspond with the measured ranges in Lemery et al. (2007) (cf., 44, 47–52, 58–68 and 70–80 ms for the RSPV, RIPV, LSPV and LIPV, respectively, following the subtraction of the LAT at earliest LA activation) providing an additional EP model validation. The isotropic EP simulations were conducted utilizing anisotropic monodomain conductivity tensors combined with random fiber architectures to remove the preferential conduction on the macroscopic scale.

4.4. Limitations

The proposed framework was designed to automatically generate personalized computational EP models of the LA from clinical and morphological data, while full personalization applies to the geometry only. There are inherent assumptions and limitations associated with such a challenging task discussed below.

The generation of geometrical models from coronary CTA images via statistics-based image segmentation relies on 3 assumptions. First, atrial and ventricular myocardium exhibit comparable radiodensities, i.e., voxel intensities in the myocardium of the LA and the left ventricle are similar. Second, structures in the proximity of the LA have different voxel intensities such that an epicardial boundary of the LA can be detected. Third, a sufficiently thick myocardial wall in the LA assumed to be minimum 1 voxel so that partial volume effects and motion artifacts have a negligible impact on the estimate of the myocardium. Despite these assumptions, estimated anatomical wall thicknesses in our models are comparable with manual measurements in CT images (Whitaker et al., 2016). Improvements in current CT technology, in particular the increased use of dual energy source scanners, will result in increased image resolution and soft tissue contrast. This will further minimize the impact of errors introduced by these assumptions.

The complex left atrial fiber architecture was qualitatively estimated based on morphological images as opposed to measured from micro-CT (Varela et al., 2013; Zhao et al., 2015; Stephenson et al., 2017), diffusion tensor MRI (Pashakhanloo et al., 2016) or contrast-enhanced MRI (Zhao et al., 2017). Distinct challenges arise when attempting to assess the atrial fiber structure using diffusion tensor MRI due to cardiac motion and a thin-walled atrial phenotype, hence this has only been performed *ex vivo*, where an interpatient analysis has demonstrated that the main features of the fiber orientation are preserved (Pashakhanloo et al., 2016). The proposed algorithm was developed to represent all prominent fiber

structures, but some degree of simplification was required. The fiber architecture in the septal portion of the LA, in particular the right atrial portion, is highly complex and subjected to large inter-patient variability making it impossible to define a standard myofiber orientation. Therefore, a continuation of the fiber direction present in the anterior right atrial septum was chosen as a standardization strategy. In goat models the presence of persistent AF altered the myofiber architecture of the LA (Maesen et al., 2013), while in a limited number of human atria no significant change in the myofiber architecture was observed between AF patients and patients with no specific atrial pathology (Pashakhanloo et al., 2016). Further measurements of the fiber orientation in AF patients are required to confirm and quantify potential changes associated with AF.

Homogeneous EP at the cellular and tissue level was assumed throughout the LA providing standardized FE simulation conditions isolating the effect of the transmural fiber architecture. Different regions in the LA such as the BB, PVs, LAA and MV exhibit distinct electrophysiological properties and would need to be included to obtain a more physiological activation pattern (Dössel et al., 2012). In addition, a single electrical stimulus was applied in the area of the BB, while the electrical signal might enter the LA on multiple sites (Markides et al., 2003). The novel pipeline focused on the LA, arguably the simpler atrium in terms of anatomy and fiber architecture, however, its critical role in AF made it the focus of attention.
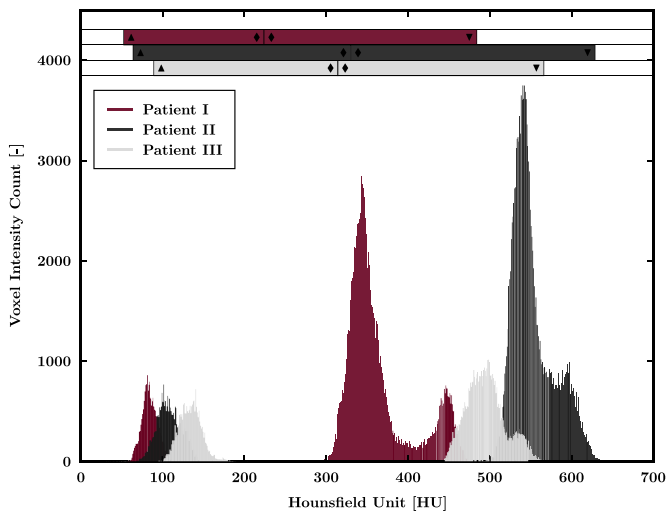
5. Conclusion

The presented modeling pipeline to generate detailed personalized computational models for left atrial EP requires a minimum degree of manual intervention facilitating the consistent development of both surface and volumetric FE models including the heterogeneous myocardial wall thickness. The complex left atrial fiber architecture within the 3-dimensional FE models derived from clinical data was estimated using a novel algorithm and qualitatively represents the most dominant fiber structures visible in morphological studies. The influence of the transmural fiber orientation on the LAT was investigated utilizing EP simulations and only minor differences were observed suggesting a negligible effect.

Appendix A. Voxel intensity histograms

Fig. A1. Voxel intensity histograms of the combined 6 sample regions (3 sample regions in each, the atrial blood pool and the left ventricular myocardium) for all patients. The superimposed bars diagrams indicate the calculated personalized intensity thresholds of the left atrial myocardium (▲ - ♦) and the left atrial cavity (♦ - ▼).

References

Adeniran, I., MacIver, D.H., Garratt, C.J., Ye, J., Hancox, J.C., Zhang, H., 2015. Effects of persistent atrial fibrillation-induced electrical remodeling on atrial electro-mechanics - Insights from a 3D model of the human atria. PloS ONE 10 (11), e0142397.

Ahn, S.S., Kim, Y.-J., Hur, J., Lee, H.-J., Kim, T.H., Choe, K.O., Choi, B.W., 2009. CT detection of subendocardial fat in myocardial infarction. American Journal of Roentgenology 192 (2), 532–537.

Bishop, M., Rajani, R., Plank, G., Gaddum, N., Carr-White, G., Wright, M., O'Neill, M., Niederer, S., 2016. Three-dimensional atrial wall thickness maps to inform catheter ablation procedures for atrial fibrillation. Europace 18 (3), 376–383.

Bishop, M.J., Plank, G., Burton, R.A.B., Schneider, J.E., Gavaghan, D.J., Grau, V., Kohl, P., 2010. Development of an anatomically detailed MRI-derived rabbit ventricular model and assessment of its impact on simulations of electrophysiological function. American Journal of Physiology - Heart and Circulatory Physiology 298 (2), H699–H718.

Cabrera, J.A., Ho, S.Y., Climent, V., Sánchez-Quintana, D., 2008. The architecture of the left lateral atrial wall: a particular anatomic region with implications for ablation of atrial fibrillation. European Heart Journal 29 (3), 356–362.

Cacciola, F., 2017. Triangulated surface mesh simplification. CGAL Editorial Board (Ed.). CGAL User and Reference Manual, 4.10 (ed.).

Center for Integrative Biomedical Computing, 2016. Seg3D: Volumetric Image Segmentation and Visualization. Scientific Computing and Imaging Institute. Download: http://www.seg3d.org.

Chang, S.-L., Tai, C.-T., Lin, Y.-J., Wongcharoen, W., Lo, L.-W., Lee, K.-T., Chang, S.-H., Tuan, T.-C., Chen, Y.-J., Hsieh, M.-H., Tsao, H.-M., Wu, M.-H., Sheu, M.-H., Chang, C.-Y., Chen, S.-A., 2007. The role of left atrial muscular bundles in catheter ablation of atrial fibrillation. Journal of the American College of Cardiology 50 (10), 964–973.

Choi, J.-I., Ryu, K., Park, E., Benser, M.E., Jang, J.K., Lee, H.S., Lim, H.E., Pak, H.-N., Kim, Y.-H., 2010. Atrial activation time and pattern of linear triple-site vs. single-site atrial pacing after cardioversion in patients with atrial fibrillation. Europace 12 (4), 508–516.

Courtemanche, M., Ramirez, R.J., Nattel, S., 1998. Ionic mechanisms underlying human atrial action potential properties: insights from a mathematical model. American Journal of Physiology - Heart and Circulatory Physiology 275 (44), H301–H321.

Crozier, A., Augustin, C.M., Neic, A., Prassl, A.J., Holler, M., Fastl, T.E., Hennemuth, A., Bredies, K., Kuehne, T., Bishop, M.J., Niederer, S.A., Plank, G., 2016. Image-based personalization of cardiac anatomy for coupled electromechanical modeling. Annals of Biomedical Engineering 44 (1), 58–70.

Dimitri, H., Ng, M., Brooks, A.G., Kuklik, P., Stiles, M.K., Lau, D.H., Antic, N., Thornton, A., Saint, D.A., McEvoy, D., Antic, R., Kalman, J.M., Sanders, P., 2012. Atrial remodeling in obstructive sleep apnea: implications for atrial fibrillation. Heart Rhythm 9 (3), 321–327.

Donal, E., Lip, G.Y.H., Galderisi, M., Goette, A., Shah, D., Marwan, M., Lederlin, M., Mondillo, S., Edvardsen, T., Sitges, M., Grapsa, J., Garbi, M., Senior, R., Gimelli, A., Potpara, T.S., Van Gelder, I.C., Gorenek, B., Mabo, P., Lancellotti, P., Kuck, K.-H., Popescu, B.A., Hindricks, G., Habib, G., 2016. EACVI/EHRA expert consensus doc-

ument on the role of multi-modality imaging for the evaluation of patients with atrial fibrillation. European Heart Journal - Cardiovascular Imaging 17 (4), 355–383.

Dössel, O., Krueger, M.W., Weber, F.M., Wilhelms, M., Seemann, G., 2012. Computational modeling of the human atrial anatomy and electrophysiology. Medical & Biological Engineering & Computing 50 (8), 773–799.

Durrleman, S., Prastawa, M., Charon, N., Korenberg, J.R., Joshi, S., Gerig, G., Trouvé, A., 2014. Morphometry of anatomical shape complexes with dense deformations and sparse parameters. NeuroImage 101, 35–49.

Fastl, T.E., Tobon-Gomez, C., Crozier, W.A., Whitaker, J., Rajani, R., McCarthy, K.P., Sanchez-Quintana, D., Ho, S.Y., O'Neill, M.D., Plank, G., Bishop, M.J., Niederer, S.A., 2016. Personalized modeling pipeline for left atrial electromechanics. Computing in Cardiology 43, 225–228.

Ferrer, A., Sebastián, R., Sánchez-Quintana, D., Rodríguez, J.F., Godoy, E.J., Martínez, L., Saiz, J., 2015. Detailed anatomical and electrophysiological models of human atria and torso for the simulation of atrial activation. PloS ONE 10 (11), e0141573.

Gonzales, M.J., Sturgeon, G., Krishnamurthy, A., Hake, J., Jonas, R., Stark, P., Rappel, W.-J., Narayan, S.M., Zhang, Y., Segars, W.P., McCulloch, A.D., 2013. A three-dimensional finite element model of human atrial anatomy: new methods for cubic hermite meshes with extraordinary vertices. Medical Image Analysis 17 (5), 525–537.

Harrild, D.M., Henriquez, C.S., 2000. A computer model of normal conduction in the human atria. Circulation Research 87 (7), e25–e36.

Hermosillo, B.D.F., 2008. Semi-automatic enhancement of atrial models to include atrial architecture and patient specific data: for biophysical simulations. Computers in Cardiology 35, 633–636.

Ho, S.Y., Anderson, R.H., Sánchez-Quintana, D., 2002. Atrial structure and fibres: morphologic bases of atrial conduction. Cardiovascular Research 54 (2), 325–336.

Ho, S.Y., Sánchez-Quintana, D., 2009. The importance of atrial structure and fibers. Clinical Anatomy 22 (1), 52–63.

Ho, S.Y., Sanchez-Quintana, D., Cabrera, J.A., Anderson, R.H., 1999. Anatomy of the left atrium: implications for radiofrequency ablation of atrial fibrillation. Journal of Cardiovascular Electrophysiology 10 (11), 1525–1533.

Hunter, R.J., Liu, Y., Lu, Y., Wang, W., Schilling, R.J., 2012. Left atrial wall stress distribution and its relationship to electrophysiologic remodeling in persistent atrial fibrillation. Circulation: Arrhythmias and Electrophysiology 5 (2), 351–360.

Jacquemet, V., Virag, N., Ihara, Z., Dang, L., Blanc, O., Zozor, S., Vesin, J.-M., Kappenberger, L., Henriquez, C., 2003. Study of unipolar electrogram morphology in a computer model of atrial fibrillation. Journal of Cardiovascular Electrophysiology 14 (S10), S172–S179.

Jernigan, S.R., Buckner, G.D., Eischen, J.W., Cormier, D.R., 2007. Finite element modeling of the left atrium to facilitate the design of an endoscopic atrial retractor. Journal of Biomechanical Engineering 129 (6), 825–837.

Krueger, M.W., Schmidt, V., Tobón, C., Weber, F.M., Lorenz, C., Keller, D.U.J., Barschdorf, H., Burdumy, M., Neher, P., Plank, G., Rhode, K., Seemann, G., Sanchez-Quintana, D., Saiz, J., Razavi, R., Dössel, O., 2011. Modeling atrial fiber orientation in patient-specific geometries: a semi-automatic rule-based approach. In: Metaxas, D.N., Axel, L. (Eds.), Functional Imaging and Modeling of the Heart. Springer, Berlin, Heidelberg, pp. 223–232.

Krueger, M.W., Seemann, G., Rhode, K., Keller, D.U.J., Schilling, C., Arujuna, A., Gill, J., O'Neill, M.D., Razavi, R., Dössel, O., 2013. Personalization of atrial anatomy and electrophysiology as a basis for clinical modeling of radio-frequency-ablation of atrial fibrillation. IEEE Transactions on Medical Imaging 32 (1), 73–84.

Labarthe, S., Coudiere, Y., Henry, J., Cochet, H., 2012. A semi-automatic method to construct atrial fibre structures: a tool for atrial simulations. Computing in Cardiology 39, 881–884.

Labarthe, S., Vigmond, E., Coudière, Y., Henry, J., Cochet, H., Jaïs, P., 2013. A computational bilayer surface model of human atria. In: Ourselin, S., Rueckert, D., Smith, N. (Eds.), Functional Imaging and Modeling of the Heart. Springer, Berlin, Heidelberg, pp. 27–34.

Lemery, R., Birnie, D., Tang, A.S.L., Green, M., Gollob, M., Hendry, M., Lau, E., 2007. Normal atrial activation and voltage during sinus rhythm in the human heart: an endocardial and epicardial mapping study in patients with a history of atrial fibrillation. Journal of Cardiovascular Electrophysiology 18 (4), 402–408.

Maesen, B., Zeemering, S., Afonso, C., Eckstein, J., Burton, R.A.B., Van Hunnik, A., Stuckey, D.J., Tyler, D., Maessen, J., Grau, V., Verheule, S., Kohl, P., Schotten, U., 2013. Rearrangement of atrial bundle architecture and consequent changes in anisotropy of conduction constitute the 3-dimensional substrate for atrial fibrillation. Circulation: Arrhythmias and Electrophysiology 6 (5), 967–975.

Markides, V., Schilling, R.J., Ho, S.Y., Chow, A.W.C., Davies, D.W., Peters, N.S., 2003. Characterization of left atrial activation in the intact human heart. Circulation 107 (5), 733–739.

McDowell, K.S., Vadakkumpadan, F., Blake, R., Blauer, J., Plank, G., MacLeod, R.S., Trayanova, N.A., 2012. Methodology for patient-specific modeling of atrial fibrosis as a substrate for atrial fibrillation. Journal of Electrocardiology 45 (6), 640–645.

McDowell, K.S., Vadakkumpadan, F., Blake, R., Blauer, J., Plank, G., MacLeod, R.S., Trayanova, N.A., 2013. Mechanistic inquiry into the role of tissue remodeling in fibrotic lesions in human atrial fibrillation. Biophysical Journal 104 (12), 2764–2773.

McDowell, K.S., Zahid, S., Vadakkumpadan, F., Blauer, J., MacLeod, R.S., Trayanova, N.A., 2015. Virtual electrophysiological study of atrial fibrillation in fibrotic remodeling. PloS ONE 10 (2), e0117110.

Mendonca Costa, C., Hoetzl, E., Martins Rocha, B., Prassl, A.J., Plank, G., 2013. Automatic parameterization strategy for cardiac electrophysiology simulations. Computing in Cardiology 40, 373–376.

Moyer, C.B., Norton, P.T., Ferguson, J.D., Holmes, J.W., 2015. Changes in global and regional mechanics due to atrial fibrillation: insights from a coupled finite-element and circulation model. Annals of Biomedical Engineering 43 (7), 1600–1613.

Niederer, S.A., Plank, G., Chinchapatnam, P., Ginks, M., Lamata, P., Rhode, K.S., Rinaldi, C.A., Razavi, R., Smith, N.P., 2011. Length-dependent tension in the failing heart and the efficacy of cardiac resynchronization therapy. Cardiovascular Research 89 (2), 336–343.

Pashakhanloo, F., Herzka, D.A., Ashikaga, H., Mori, S., Gai, N., Bluemke, D.A., Trayanova, N.A., McVeigh, E.R., 2016. Myofiber architecture of the human atria as revealed by submillimeter diffusion tensor imaging. Circulation: Arrhythmias and Electrophysiology 9 (4), e004133.

Rahman, F., Kwan, G.F., Benjamin, E.J., 2014. Global epidemiology of atrial fibrillation. Nature Reviews Cardiology 11 (11), 639–654.

Rodríguez-Granillo, G.A., Rosales, M.A., Degrossi, E., Rodriguez, A.E., 2010. Signal density of left ventricular myocardial segments and impact of beam hardening artifact: implications for myocardial perfusion assessment by multidetector CT coronary angiography. International Journal of Cardiovascular Imaging 26 (3), 345–354.

Satriano, A., Bellini, C., Vigmond, E.J., Di Martino, E.S., 2013. A feature-based morphing methodology for computationally modeled biological structures applied to left atrial fiber directions. Journal of Biomechanical Engineering 135 (3), 031001.

Schotten, U., Verheule, S., Kirchhof, P., Goette, A., 2011. Pathophysiological mechanisms of atrial fibrillation: a translational appraisal. Physiological Reviews 91 (1), 265–325.

Seemann, G., Höper, C., Sachse, F.B., Dössel, O., Holden, A.V., Zhang, H., 2006. Heterogeneous three-dimensional anatomical and electrophysiological model of human atria. Philosophical Transactions of the Royal Society A: Mathematical, Physical and Engineering Sciences 364 (1843), 1465–1481.

Stephenson, R.S., Atkinson, A., Kottas, P., Perde, F., Jafarzadeh, F., Bateman, M., Iaizzo, P.A., Zhao, J., Zhang, H., Anderson, R.H., Jarvis, J.C., Dobrzynski, H., 2017. High resolution 3-dimensional imaging of the human cardiac conduction system from microanatomy to mathematical modeling. Scientific Reports 7 (1), 7188.

Teh, A.W., Kistler, P.M., Lee, G., Medi, C., Heck, P.M., Spence, S.J., Sparks, P.B., Morton, J.B., Kalman, J.M., 2012. Electroanatomic remodeling of the left atrium in paroxysmal and persistent atrial fibrillation patients without structural heart disease. Journal of Cardiovascular Electrophysiology 23 (3), 232–238.

Tobón, C., Ruiz-Villa, C.A., Heidenreich, E., Romero, L., Hornero, F., Saiz, J., 2013. A three-dimensional human atrial model with fiber orientation. Electrograms and arrhythmic activation patterns relationship. PloS ONE 8 (2), e50883.

Tobon-Gomez, C., Geers, A.J., Peters, J., Weese, J., Pinto, K., Karim, R., Ammar, M., Daoudi, A., Margeta, J., Sandoval, Z., Stender, B., Zheng, Y., Zuluaga, M.A., Betancur, J., Ayache, N., Chikh, M.A., Dillenseger, J.-L., Kelm, B.M., Mahmoudi, S., Ourselin, S., Schlaefer, A., Schaeffter, T., Razavi, R., Rhode, K.S., 2015. Benchmark for algorithms segmenting the left atrium from 3D CT and MRI datasets. IEEE Transactions on Medical Imaging 34 (7), 1460–1473.

Trayanova, N.A., 2014. Mathematical approaches to understanding and imaging atrial fibrillation: significance for mechanisms and management. Circulation Research 114 (9), 1516–1531.

Trayanova, N.A., Chang, K.C., 2016. How computer simulations of the human heart can improve anti-arrhythmia therapy. The Journal of Physiology 594 (9), 2483–2502.

Varela, M., Colman, M.A., Hancox, J.C., Aslanidi, O.V., 2016. Atrial heterogeneity generates re-entrant substrate during atrial fibrillation and anti-arrhythmic drug action: mechanistic insights from canine atrial models. PLoS Computational Biology 12 (12), e1005245.

Varela, M., Morgan, R., Theron, A., Dillon-Murphy, D., Chubb, H., Whitaker, J., Henningsson, M., Aljabar, P., Schaeffter, T., Kolbitsch, C., Aslanidi, O.V., 2017. Novel MRI technique enables non-invasive measurement of atrial wall thickness. IEEE Transactions on Medical Imaging 36 (8), 1607–1614.

Varela, M., Zhao, J., Aslanidi, O.V., 2013. Determination of atrial myofibre orientation using structure tensor analysis for biophysical modelling. In: Ourselin, S., Rueckert, D., Smith, N. (Eds.), Functional Imaging and Modeling of the Heart. Springer, Berlin, Heidelberg, pp. 425–432.

Vigmond, E.J., Hughes, M., Plank, G., Leon, L.J., 2003. Computational tools for modeling electrical activity in cardiac tissue. Journal of Electrocardiology 36 (S), 69–74.

Vigmond, E.J., Ruckdeschel, R., Trayanova, N., 2001. Reentry in a morphologically realistic atrial model. Journal of Cardiovascular Electrophysiology 12 (9), 1046–1054.

Vigmond, E.J., Weber dos Santos, R., Prassl, A.J., Deo, M., Plank, G., 2008. Solvers for the cardiac bidomain equations. Progress in Biophysics and Molecular Biology 96 (1–3), 3–18.

Werner, C.D., Sachse, F.B., Dössel, O., 2000. Electrical excitation propagation in the human heart. International Journal of Bioelectromagnetism 2 (2).

Whitaker, J., Rajani, R., Chubb, H., Gabrawi, M., Varela, M., Wright, M., Niederer, S., O'Neill, M.D., 2016. The role of myocardial wall thickness in atrial arrhythmogenesis. Europace 18 (12), 1758–1772.

Zemlin, C.W., Herzel, H., Ho, S.Y., Panfilov, A., 2001. A realistic and efficient model of excitation propagation in the human atria. In: Virag, N., Blanc, O., Kappenberger, L. (Eds.), Computer Simulation and Experimental Assessment of Cardiac Electrophysiology. Futura Publishing Company, Inc., Armonk, pp. 29–34.

Zhang, L.T., Gay, M., 2008. Characterizing left atrial appendage functions in sinus rhythm and atrial fibrillation using computational models. Journal of Biomechanics 41 (11), 2515–2523.

Zhao, J., Butters, T.D., Zhang, H., LeGrice, I.J., Sands, G.B., Smaill, B.H., 2013. Image-based model of atrial anatomy and electrical activation: a computational platform for investigating atrial arrhythmia. IEEE Transactions on Medical Imaging 32 (1), 18–27.

Zhao, J., Butters, T.D., Zhang, H., Pullan, A.J., LeGrice, I.J., Sands, G.B., Smaill, B.H., 2012. An image-based model of atrial muscular architecture: effects of structural anisotropy on electrical activation. Circulation: Arrhythmias and Electrophysiology 5 (2), 361–370.

Zhao, J., Hansen, B.J., Csepe, T.A., Lim, P., Wang, Y., Williams, M., Mohler, P.J., Janssen, P.M.L., Weiss, R., Hummel, J.D., Fedorov, V.V., 2015. Integration of high-resolution optical mapping and 3-dimensional micro-computed tomographic imaging to resolve the structural basis of atrial conduction in the human heart. Circulation: Arrhythmias and Electrophysiology 8 (6), 1514–1517.

Zhao, J., Hansen, B.J., Wang, Y., Csepe, T.A., Sul, L.V., Tang, A., Yuan, Y., Li, N., Bratasz, A., Powell, K.A., Kilic, A., Mohler, P.J., Janssen, P.M.L., Weiss, R., Simonetti, O.P., Hummel, J.D., Fedorov, V.V., 2017. Three-dimensional integrated functional, structural, and computational mapping to define the structural "fingerprints" of heart-specific atrial fibrillation drivers in human heart ex vivo. Journal of the American Heart Association 6 (8), e005922.